1
Wave–Particle Duality of the Neutron

1.1
Discovery of Matter Waves

The fundamental fact that every particle with mass is at the same time a wave was discovered in 1925 by *de Broglie* [1]. He was honored with the award of the Nobel Prize for Physics in 1929 for this discovery. We begin our study of neutron optics with his proof of *the matter wave* following his Nobel lecture [2].

De Broglie was of the opinion that to solve the new serious question in physics that arose around 1900, the unification of matter and radiation was necessary, and more practically said that it should be possible to establish the equality of corpuscular motion and wave propagation. As the simplest case, he assumed a system consisting of a corpuscle at rest and completely free from all outside influence, and expressed the system as $\circ x_0 y_0 z_0$. In the sense of Einstein's relativity principle, we can consider this system being the "intrinsic" system of the corpuscle. Since the corpuscle is steady and at rest, the phase of the wave we are now considering must be the same at every point; that is, it can be expressed in the form $\sin[2\pi\nu_0(t_0-\tau_0)]$, where t_0 is the intrinsic time for the corpuscle and τ_0 is a constant.

As the next step, according to the principle of inertia, in every Galilean system we can make the corpuscle have linear motion and constant velocity. Let us consider such a Galilean system where the corpuscle has velocity $v = \beta c$. We will not lose generality by taking the x-axis as the direction of motion. According to the Lorentz transformation, the time t elapsing for the observer in this new system will be related to the intrinsic time t_0 defined above through the equation

$$t_0 = \frac{t - \frac{\beta x}{c}}{\sqrt{1-\beta^2}}\,, \tag{1.1}$$

and therefore the phase of the wave for the present observer will be given by

$$\sin\left[2\pi\frac{\nu_0}{\sqrt{1-\beta^2}}\left(t - \frac{\beta x}{c} - \tau_0\right)\right]. \tag{1.2}$$

Therefore, for the observer the wave will now have frequency

$$\nu = \frac{\nu_0}{\sqrt{1-\beta^2}}\,, \tag{1.3}$$

Neutron Optics. Masahiko Utsuro,Vladimir K. Ignatovich

ISBN: 978-3-527-40885-6

and will then propagate in the direction of the x-axis with *phase velocity*

$$V = \frac{c}{\beta} = \frac{c^2}{v} . \tag{1.4}$$

On the other hand, we can define *the group velocity* U for the wave as the velocity corresponding to the resultant amplitude from a group with very similar frequencies, and according to Rayleigh's definition for this velocity, $U = \partial\omega/\partial k$, where the wave number $k = 2\pi v/V$, it satisfies the equation

$$\frac{1}{U} = \frac{\partial\left(\frac{v}{V}\right)}{\partial v} = \frac{1}{v} . \tag{1.5}$$

In this way, we obtain the very important relation for the development of the present theory that the group velocity for the waves in the system $x\,y\,z\,t$ is equal to the velocity of the corpuscle.

To achieve our purpose to establish the equality of the corpuscle and the wave, we must combine the energy and the quantity of the motion. In the same way as in the previous Galilean transformation,

$$\text{Energy} = h \times \text{frequency} , \quad \text{or} \quad W = hv , \tag{1.6}$$

where h is Planck's constant. This relation reduces further according to the Einstein relation to its internal energy m_0c^2 in the intrinsic system as

$$hv_0 = m_0c^2 , \tag{1.7}$$

where m_0 is the rest mass. Since the quantity of movement, that is, the momentum, $\boldsymbol{p}$, has magnitude equal to $m_0v/\sqrt{1-\beta^2}$, then

$$p = |\boldsymbol{p}| = \frac{m_0v}{\sqrt{1-\beta^2}} = \frac{Wv}{c^2} = \frac{hv}{V} = \frac{h}{\lambda}, \tag{1.8}$$

where the quantity λ is defined as the distance between two consecutive peaks of the wave (which corresponds to the phase velocity divided by the frequency), that is, *the wavelength*. In this way, we obtain the very important relation

$$\lambda = \frac{h}{p} . \tag{1.9}$$

This is *de Broglie's fundamental formula*.

De Broglie's matter wave was experimentally verified in the first place by Davisson and Thomson with *the discovery of the diffraction of electrons* [3, 4], and they were also awarded the Nobel Prize for Physics, in 1937. A few months after their experiment, Kikuchi reported the characteristic pattern of electron diffraction owing to the effects of thermal diffuse scattering from crystals (the so-called *Kikuchi pattern*) [5], and made an important contribution to the establishment of quantum mechanics developed by Heisenberg [6].

Pauli's textbook of quantum mechanics [A] starts with the following description: *The last decisive turning point of quantum theory came with de Broglie's hypothesis of matter waves, Heisenberg's discovery of matrix mechanics, and Schrödinger's wave equation, the last establishing the relationship between the first two sets of ideas.*[1)]

1.2 Proof of the Wave Nature of the Neutron

1.2.1 Bragg Reflection

Chadwick's discovery of the neutron in 1932 [7, 8] soon motivated the experimental verification of its *wave nature*. The approach is the same as that for the first proof on the matter wave of the electron, where *Bragg scattering* was observed [3, 4], but for the neutron, with a much larger mass and essentially no electric charge, it has significant advantages in view of the energy condition and of the electromagnetic effects in crystals. Actually, the wavelength calculated with Eq. (1.9) for neutrons with energy corresponding to room temperature (so-called *thermal neutrons*) is of the same order as the lattice spacing in most simple crystals, about 0.2 nm ($1\,\text{nm} = 10^{-9}\,\text{m} = 10\,\text{Å}$), and those neutrons that easily penetrate inside a crystal can be scattered directly by nuclei in the crystal, resulting in obvious *Bragg reflections*. As an example of such experiments, Mitchell and Powers [9] irradiated a single crystal of MgO with the neutron beam extracted from a paraffin moderator in which a Rn–Be neutron source was embedded, and they considered the contribution to the counting rate due to Bragg scattering as proof of the existence of a coherent component in nuclear scattering by the crystal nuclei.

However, the epoch-making event to initiate drastic developments of various kinds of neutron experiments was the realization of the first nuclear chain reaction in the reactor CP-1 conducted by Fermi in 1942. Furthermore, the first heavy water reactor, CP-3 in 1944, opened the door to precise neutron experiments by using a high-intensity neutron beam. Zinn [10] used the experimental devise shown in Figure 1.1a and reported for the first time a very clear distribution of Bragg-scattered neutrons, as shown in Figure 1.1b.

Thermal neutrons extracted from a reentrant hole in the graphite thermal column of the heavy water reactor are well collimated through an iron collimater in the reactor shielding and a couple of thick cadmium slits outside the shielding, and illuminate the single crystal on a rotating sample table. The neutrons scattered by the sample are registered by the BF_3 proportional counter at the end of the precisely rotating arm of a large mechanical device. The sample table and the counter arm are driven exactly with a 1 : 2 angular ratio. The results obtained on the sample of

1) Schrödinger followed de Broglie's idea of matter waves in setting up his equation. Later he proved the equivalence of his approach and that of Heisenberg.

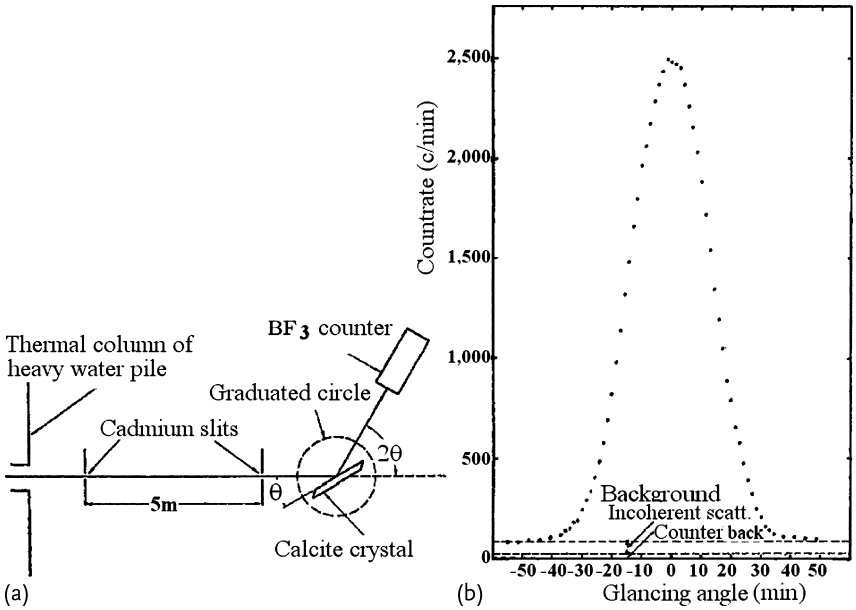

Figure 1.1 The first obvious measurement of Bragg-scattered neutrons. (a) Experimental setup; (b) a typical rocking curve of reflected neutrons measured on the (1,0,0) plane of a LiF crystal (Zinn [10]).

a LiF single crystal are given in Figure 1.1b. The distribution indicated is shown before the corrections for the detector efficiency and the energy resolution of the setup, and therefore a slight asymmetry is noticed. The apparatus was also used for measuring the energy distribution of incident thermal neutrons by replacing the sample with a larger single crystal of calcite, as shown in Figure 1.1a.

Furthermore, the whole apparatus was moved to a beam hole inserted directly in the reactor core, and was used for nuclear cross section measurements in a wider energy range, including *epithermal neutrons.*[2)]

Such neutron experiments, a typical setup for which is shown in Figure 1.1, proved that the diffraction experiment is possible using a device and setup quite similar to those for X-rays. However, in contrast to X-rays scattered mainly by atomic electrons, neutrons are mainly scattered or absorbed by the nucleus, and therefore quite different materials are utilized for radiation shielding for neutrons.

After these initial developments, neutron spectroscopy experiments made great progress, and nowadays various kinds of neutron spectrometers are used in experiments applied to a wide variety of samples, including crystalline solids, alloys,

2) Those neutrons with energy higher than the room temperature Maxwellian distribution but lower than the resonance region for nuclear reactions; that is, the energy region of about 0.1–1 eV.

complicated compounds, polymers, and biological material. Typical cases of these applications will be given in the last two chapters.

Among these spectroscopies, the method based on Bragg scattering with crystals called *crystal spectrometry* is one of the most popular and important approaches. The relation for the spectroscopic resolution can be derived from the well-known *Bragg law* on the neutron wavelength λ of Bragg scattering for lattice spacing d and neutron incident angle θ of the crystal:

$$n\lambda = 2d\sin\theta\ , \quad \text{or} \quad \tau = 2k\sin\theta\ , \tag{1.10}$$

where $\tau = 2\pi n/d$, $k = 2\pi/\lambda$, and n is an integer. Differentiation of both sides of the logarithm of Eq. (1.10) and the expression for the neutron energy E,

$$E = \frac{\hbar^2}{2m}k^2 = \frac{\hbar^2}{2m}\left(\frac{2\pi}{\lambda}\right)^2\ , \tag{1.11}$$

lead to

$$\Delta E/E \cong 2\Delta k/k \cong 2[(\Delta\tau/\tau)_{hkl} + \cot\theta\,\Delta\theta]\,, \tag{1.12}$$

where τ_{hkl} is the magnitude of the *reciprocal lattice vector* with *Miller indices* hkl for a three-dimensional crystal, and $\Delta\theta$ is the beam divergence.

This equation indicates that the highest energy resolution can be obtained by employing a Bragg angle of $\theta = \pi/2$. A novel technique based on the present principle was developed as *backscattering spectrometry* [11] for neutron scattering experiments with very fine energy resolution.

1.2.2
Refractive Index and Total Reflection

At the same time as these experimental developments, construction of an optical theory for neutrons was also carried out by taking into account the nuclear scattering, which has very different characteristics from scattering of X-rays. For the analysis of neutron optics, we must first describe the matter waves with the wavelength and the frequency given by de Broglie's fundamental formula (Eq. (1.9)) as a function of variables for practical situations. The wave function required to describe the matter wave and the related general fundamental equation in wave mechanics had already been by Schrödinger in 1926. Furthermore, in 1936 Fermi presented the simplest and most effective expression for the nuclear scattering potential to be inserted in the Schrödinger equation to obtain a solution [12, 13], the so-called *Fermi pseudopotential*, written in the form

$$V(\boldsymbol{r}) = 4\pi\sum_j b_j\,\delta(\boldsymbol{r} - \boldsymbol{r}_j)\,, \tag{1.13}$$

where b_j and $\boldsymbol{r}_j$ denote the scattering amplitude[3)] and the position, respectively, of the jth nucleus.

3) In many textbooks it is called *the scattering length*, but here we denote it *the scattering amplitude*.

Starting from these fundamental arrangements, Foldy [14], Goldberger and Seits [15], and Lax [16] analyzed the interference phenomenon for neutrons under multiple scattering in media, then the preliminary theory of neutron optics was established. The details of the theory will not be discussed here since many standard textbooks on neutron scattering (e.g., [D]–[E]) have already been published, and here only one of the useful formulas will be given for the *index of neutron refraction n*, and derived by Goldberger and Seits [15] in the case of sufficiently weak absorption and without the effects of neutron spin:

$$1 - n^2 = \pm \frac{N(4\pi\sigma_s)^{\frac{1}{2}}}{k^2} \,. \tag{1.14}$$

In Eq. (1.14), N is the atomic density, σ_s the coherent scattering cross section, k the wave number of neutrons without the medium. To determine whether the right side should be positive or negative, information about the scattering nucleus, that is, the definition of the sign of the *coherent scattering amplitude (coherent scattering length)* becomes necessary. Foldy [14] carried out general analyses including randomly distributed scatterers, and Lax [16] discussed the effects of *incoherent scattering* and of possible anisotropy in the scattering amplitude.

According to Eq. (1.14), total reflection of neutrons will happen if we select the grazing angle θ between the incident neutrons and the surface of the medium with the positive sign on the right side such as to satisfy the condition

$$\sin^2\theta \leq \sin^2\theta_c = 1 - n^2 \,. \tag{1.15}$$

In other words, whether total reflection from any material happens or does not happen for incident neutrons in a vacuum (or in atmospheric air) and, further, what the *critical angle for total reflection* θ_c is should give us information about the sign to be selected and the magnitude of the scattering amplitude $|b| = (\sigma_s/4\pi)^{1/2}$ on the right side of Eq. (1.14) for the element in the material.

Fermi and Marshall [17] modified the experimental setup shown in Figure 1.1 to the arrangement shown in Figure 1.2, where a monochromatic neutron beam with a wavelength of 0.1873 nm Bragg-reflected by the first crystal was incident on the front surface of a solid sample on the second turntable with a very small grazing angle.

The second turntable was provided with a detector arm, and the detector count rates were registered with precise alteration of the detector angle. Such a set of measurements was repeated for fine stepwise increments of the incidence angle to the sample, and clearly indicated the ending of total reflection with a sudden decrease of the reflected intensity. Thus, they obtained the values of the critical angle for total reflection on specimens of beryllium, graphite, iron, nickel, zinc, and others in the angular range of 7–12 minutes with the accuracy of about a tenth of a minute.

According to the present definition, the *refractive index formula* (1.14) and the *total reflection formula* (1.15) are reduced, respectively, to

$$n^2 = 1 - \frac{N b_{\mathrm{coh}} \lambda^2}{\pi} \tag{1.16}$$

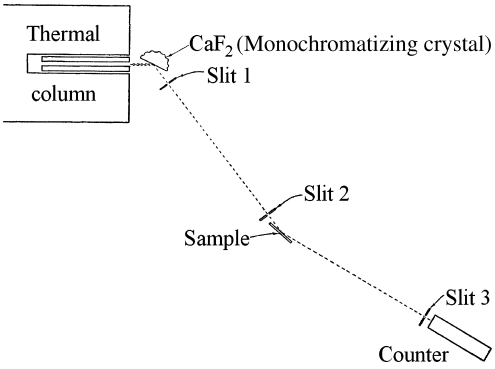

Figure 1.2 Arrangement of the total reflection experiment with a monochromatic neutron beam (Fermi and Marshall [17]).

and

$$\sin^2\theta \leq \sin^2\theta_c = \frac{N b_{\mathrm{coh}} \lambda^2}{\pi} . \tag{1.17}$$

Furthermore, the refractive index can be expressed in a more generalized form as

$$n^2 = 1 - \frac{U}{E} , \tag{1.18}$$

where U is the *optical potential* for the medium, given by

$$U = \frac{\hbar^2}{2m} 4\pi N b_{\mathrm{coh}} . \tag{1.19}$$

Lax [16], who extended the approach of Foldy [14] to the case of an anisotropic scattering amplitude, showed that the coherent scattering amplitude appearing in the *total reflection formula* (1.17) corresponds to the amplitude for forward scattering, that is, $b_{\mathrm{coh}}(\boldsymbol{a} \leftarrow \boldsymbol{a})$. Since this is a recoilless process, the value of the amplitude should not depend on the states of chemical binding. Nevertheless, it should take the value for the *bound atom scattering amplitude (scattering length)*, that is, the magnitude $b_{\mathrm{coh}} = a_{\mathrm{coh}}(A+1)/A$, where the *reduced mass factor* $(A+1)/A$ is a multiplication factor for an atom with mass number A bound to an infinite mass and a_{coh} is the amplitude of an isolated free atom.

Hughes, Burgy, and Ringo [18] proved the applicability of the total reflection formula (1.17) also for liquids; the details of their experiment are given in Section 2.1.

Furthermore, McReynolds [19] examined experimentally the applicability of the formula to samples in the gaseous state where atoms or molecules are distribute far apart from each other and are independently in free motion. The experiments were carried out at Oak Ridge and Brookhaven research reactors making use of the setup shown in Figure 1.3a. The observed total reflection intensity from the gas–liquid interface could be related to the criticality condition given by the difference

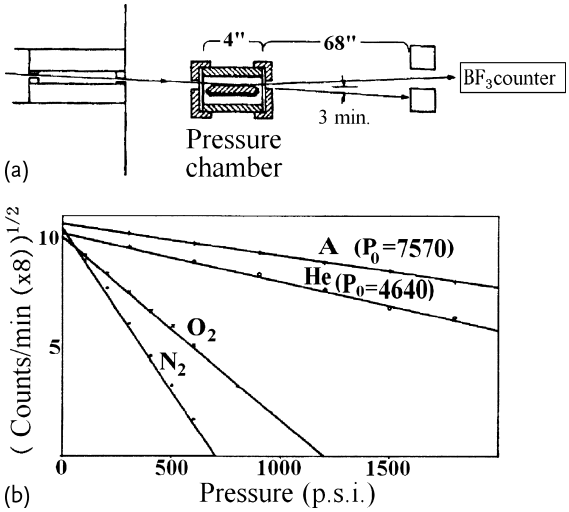

Figure 1.3 Neutron total reflection from a high-pressure gas and liquid interface: (a) experimental apparatus and (b) intensity of the neutron beam reflected from a surface of ethylene glycol at an angle of 3 minutes as a function of the surrounding gas pressure (McReynolds [19]).

between the right sides of Eq. (1.17) for the gas and the liquid, respectively. In the present experimental condition with the energy spectrum proportional to the neutron energy E, the square root of the reflected intensity I is expected to show a pressure dependence as

$$\left(\frac{I}{I_0}\right)^{\frac{1}{2}} = \frac{E_{c12}(P)}{E_{c1}} = \frac{N_1 b_{\mathrm{coh1}} - N_2 b_{\mathrm{coh2}}}{N_1 b_{\mathrm{coh1}}} = 1 - \frac{P}{P_0}\,, \tag{1.20}$$

where the subscripts 1 and 2 denote liquid and gaseous samples, respectively. Further, $E_{c12}(P)$ and E_{c1} represent the neutron energies satisfying the critical condition for the *total reflection from the gas–liquid interface* at sample pressures P and 0, respectively, whereas at pressure P_0 the refractive index for the gas becomes same as that for the liquid, and then the reflected intensity disappears. The experimental results shown in Figure 1.3b indicate the variation just as expected from Eq. (1.20).

1.2.3
Fraunhofer Diffraction

In addition to the diffraction experiments on crystal lattices and the total reflection experiments mentioned above, typical verification of the wave nature of neutrons is also possible with interference experiments using a *Fresnel biprism* or *Young's double slit* applied to neutrons. The former type of experiment was proposed and performed by Maier-Leibnitz and Springer at the FRM reactor, Technical University of Munich [20]. Their experimental results indicated an obvious interference

pattern, which corresponded as a whole with their theoretical curves, but there remained locally some delicate disagreements which could be considered to indicate the difficulty of using a biprism interferometer for neutrons [21, 22].

The first trial of the slit interference experiments was carried out by Shull as a *single-slit interference experiment* [23]. In such a single-slit interference experiment, if the slit width is much smaller than the distance L between the beam source and the slit, and the distance L' between the slit and the observation point (i.e., the condition $a/2L + a/2L' \ll \lambda/a$ is satisfied for the neutron wavelength λ used in the experiment), then the interference pattern will reduce to the so-called *Fraunhofer diffraction* in which the curvature of the wave front can be neglected, and the intensity distribution $I(\theta)$ at the diffraction angle θ should be given by the equation $I(\theta) = I_0(\sin\beta/\beta)^2$, where $\beta = (\pi a/\lambda)\sin\theta$. Shull employed a neutron wavelength of 0.443 nm and a slit width of about 4–21 μm, and observed the apparent broadening of the diffraction peak, in good agreement with the calculated result of the Fraunhofer diffraction width. His result indicated that the wave front of neutrons entering the slit has coherency over a width of at least 20 μm in the direction transverse to the propagation direction of the neutron waves.

A more distinct slit interference for neutrons could be verified in the *double-slit interference experiment* corresponding to Young's optical experiment (1801). Zeilinger *et al.* [24] performed a precise double-slit interference experiment by making use of a beam of *very cold neutrons* extracted from the high-flux research reactor at the Institut Laue–Langevin, Grenoble, and with them being monochromatized to a wavelength of about 2 nm through a prism. The experimental result was compared with the numerical calculation simulating exactly the experimental procedure according to elementary wave mechanics. The width of slit S_1 in Figure 1.4a used in the experiment was carefully adjusted according to the neutron wavelength in the experiment, whereas the width of slit S_2 and that of the incident slit S_3 and the scanning slit S_4 were fixed at 100 and 20 μm, respectively. The object slit S_5 is a double slit consisting of two open channels with a width of about 22 μm each separated by a shielded part of boron wire with a width of about 104 μm as a neutron absorber, so that neutrons transmitted through slit S_5 are spatially *split* into two optical paths. Neutrons with a wavelength 1.845 ± 0.142 nm were used in the experiment.

It will be instructive for understanding the neutron optics in the present experiment to explain some details of their simulated calculation to obtain the double-slit interference. It starts from the *Huygens principle* (1690). Considering the vertical symmetry of the arrangement shown in Figure 1.4a, we can employ a two-dimensional structure in which the wave distribution at an arbitrary point in the object slit S_5 will be constructed by the interference with the phase distribution due to the products of the wave number and the optical path length for every point in the incident slit. On the other hand, the possible difference in the attenuation effect due to the optical path length difference can be neglected when considering the statistical accuracy of the experimental result because of the much smaller value for the slit width to the path length ratio. The wave propagation from the object slit to the detector slit can also be considered in a similar way. Therefore, the intensity

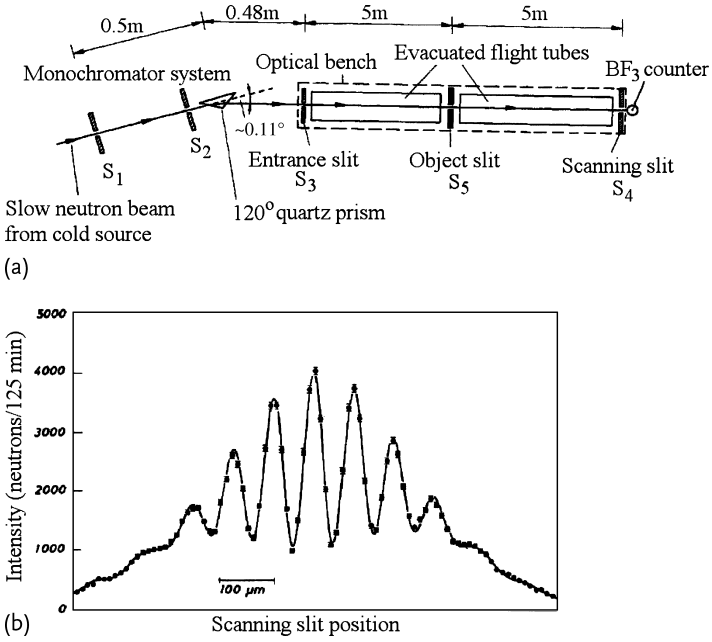

Figure 1.4 Double-slit neutron interference experiment. (a) Experimental arrangement (not to scale) and (b) experimental result compared with the theoretical calculation of the double-slit interference pattern (Zeilinger *et al.* [24]).

distribution I at an observation point P in the detector can be expressed by

$$I \propto \iiint |U(P)|^2 w(\lambda) w(\delta\vartheta) d\lambda\, d(\delta\vartheta)\, dS_4\,, \tag{1.21}$$

where the amplitude $U(P)$ at point P is given by

$$U(P) \propto \iint f(\delta\vartheta) e^{ik(r+s)} dS_3\, dS_5\,, \tag{1.22}$$

k is the neutron wave number, r and s are the optical path lengths in the diffraction plane from the incident point to a point in the object slit and from there to the detection point, respectively, and $w(\lambda)$, $w(\delta\theta)$, and $f(\delta\vartheta)$ are the wavelength and angular distributions of incident neutrons, and the factor to take into consideration the relative phase at an incident point induced by the incident wave in the angle $\delta\vartheta$, respectively.

Equation (1.22) giving the amplitude $U(P)$ produced at point P by an incident plane wave is the integration as a coherent superposition, whereas Eq. (1.21), integrating over the incident wavelength and angular distributions, is simply the intensity integral as an incoherent superposition. The result of the present numerical calculation considering the slight asymmetry in two slit widths based on the actually observed result from optical microscopy shows very good agreement with the

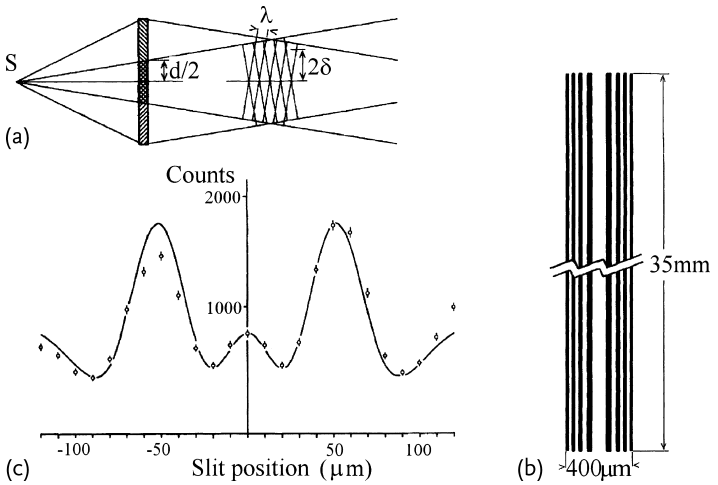

Figure 1.5 Split-lens interferometer configuration for neutrons: (a) principle of an overlapping split-zone plate working as a lens giving a constant fringe spacing; (b) split-lens geometrical pattern as a cylindrical zone plate preferable to a pinhole source for photomicrolithography; and (c) experimental interference pattern for a Cu zone plate fitted to the theoretical pattern for a zone thickness of 1.3 μm (Klein *et al.* [25]).

experimental result in Figure 1.4b, and the slit widths derived from the calculation gave values near those of the microscopy results. However, from the single-slit experiment carried out in a similar way with a slit width of about 95 μm, the slit width that gave the best fit was about 5% larger in comparison with the the microscopy result and the mechanical measurement with spacers, and this disagreement could not be explained well [24].

1.2.4
Fresnel Diffraction

All the slit interferences mentioned above are phenomena belonging the Fraunhofer diffraction; therefore, at the end of this section a few examples will be given for *Fresnel diffraction*, where the curvature of the wave front plays an important role in the interference. For the diffracting elements in such an experiment, a crystal restricts the neutron wavelength to below the Bragg cutoff, and a prism is also not preferable to focus on a short distance in the case of neutrons with a refractive index n very near unity ($|n-1| \sim 10^{-4}$ for a wavelength of 2 nm). Therefore, Klein *et al.* [25] employed a *Fresnel zone plate* and verified its applicability as an approach for the Fresnel diffraction of *cold neutrons* with a wavelength of 0.5–2 nm and *very cold neutrons* with a wavelength of about 2–30 nm.

In the *split-lens interferometer* configuration shown in Figure 1.5a, two kinds of zone plates, the central parts of where are overlapping, diffract the waves from the primary source S inward, and as the result is a fringe with a constant spacing in

the region where the wave fronts overlap. They employed refractive zone plates to produce fringes with a *phase shift due to the refractive index* according to Eqs. (1.14)–(1.17), instead of ordinary absorption zone plates, for higher luminosity and applicability for neutrons with a refractive index very near unity. Further, they used the cylindrical zone plates illustrated in Figure 1.5b, which are preferable to a pinhole primary source as in the case of a narrow slit to be arranged in a neutron facility. They prepared such zone plates by means of photomicrolithographic techniques with UV light photography from the geometric patterns illustrated in Figure 1.5b, and then photoresists masked the electrolytic deposition. The required thickness $D(\lambda/2)$ for the wavelength λ to give a phase shift of 180°, that is, $\lambda/2$, can be estimated as

$$D\left(\frac{\lambda}{2}\right) = \frac{\lambda}{2(1-n)} \cong \frac{\pi}{N b_{\mathrm{coh}} \lambda}\,, \tag{1.23}$$

from which they used $D(\lambda/2) = 2.4$ μm for copper at a wavelength of 2 nm. One of the experimental results of the *interference experiments with such split-zone plates* of electrodeposited copper carried out at the Grenoble high-flux reactor is shown in Figure 1.5c. The experimental fringe spacing δ agreed well with the theoretically estimated value of 51.8 μm from the equation

$$\delta = \frac{\lambda[f\rho - r(\rho - f)]}{\rho d}\,, \tag{1.24}$$

where the experimental wavelength $\lambda = 1.93 \pm 0.05$ nm, and f, ρ, and r are the focal length, the distances from the lens to the source, and the distance to the plane of detection, respectively, all being 5 m. Further detailed theoretical calculations indicated that the interference pattern corresponded to a copper thickness of 1.3 μm in the zone plates. This experiment verified the technical advantages of the interference experiments with split-zone plates, whereas the close spacing of the interfering beams would restrict the application of the method.

On the other hand, Steyerl *et al*. analyzed three-dimensional focusing with constructive interference of long-wavelength neutrons and designed an achromatic *concave Fresnel zone mirror* for ultracold neutrons [26]. The image formation experiment was carried out on such a circular zone ring mirror electrodeposited on an aspherical concave substrate with 60–80 nm *ultracold neutrons* at the inclined and highly curved guide facility PN5 of the Grenoble reactor. The experimental result agreed with the theoretical expectation at a magnification of 5 within the statistical error [27].

As mentioned above, the phenomenon of de Broglie matter waves of neutrons without consideration of the spin is considered to be precisely described by the law of *scalar optics*, where the amplitude and the phase of waves are exactly and uniquely decided by the position and the time.

However, a further advanced question that will arise quite naturally is if once split waves as considered in this section are superposed again at some position, how great a shift in the space or in the time is allowed to maintain the coherence of the waves. Such kinds of studies on the coherence of waves will be presented in the next section and in later chapters.

In addition to Bragg scattering and slit interferences or zone mirrors used in the historical experiments which verified the wave nature of neutrons, various types of neutron interferometers, such as Mach–Zehnder, Fabry–Pérot, and Jamin types, were also developed. These studies will also be introduced and discussed in Chapter 9. In Chapters 2 and 6, neutron optical experiments in various structures and systems will be described. As the neutron has spin, in some kinds of experiments the spin must be taken into consideration as a new variable, and such experiments relating to the neutron spin will be mainly discussed in Chapter 3 after a short preliminary study in the last section of this chapter.

1.3 Coherence of Waves

1.3.1 Coherence Lengths

In the theoretical calculation (Figure 1.4b) of Zeilinger *et al*. described in the previous section with the exact wave mechanical simulation of the double-slit interference [24], the integrals (1.21) and (1.22) were classified as the *coherent superposition*, Eq. (1.22), and the *incoherent intensity integral*, Eq. (1.21), over the wave components propagating downstream from each incident point. This classification was decided on depending on whether a certain correlation exists or does not exist between the phases of different partial waves, as the former belongs to the case without any accompanying random phase shift, whereas the latter belongs to the case with some accompanying random phase shifts. Since there is currently no coherent primary source for neutrons realized as there is laser light sources, superposition of waves for a couple of free neutrons should also belong to the latter case.

Since the monochromatization of incident neutrons in the experiment of Zeilinger *et al*. was performed with the combination of fine slits and a prism at a position sufficiently far from the primary source as shown in Figure 1.4a, the coherent superposition could be well approximated by the optical path integral, Eq. (1.22), of monochromatic plane *partial waves* owing to the prism having a different refraction angle for different wavelengths. In contrast, in the case of monochromatization with Bragg scattering, the correct relation between the wave components with different wavelengths and their coherence could not be represented so simply, but both of the quality of the monochromator crystal and the experimental setup must be taken into consideration.

For example, in the monochromatization setup for neutron scattering, a *mosaic crystal* which consists of a number of microcrystals with slightly different orientations is often used to obtain the optimum beam intensity by reflecting a rather wide wavelength range and over wide angular regions. *Pyrolytic graphite* is one such imperfect crystal that is nearly ideal for broad-angle monochromatization [28]. A recent study on pyrolytic graphite reported, in addition to such mosaicity, a distribution width in the lattice spacing, which induces additional broadening in

the Bragg-scattered wavelength width [29]. When such a component is used in a neutron optics experiment such as interferometry, the wave phenomena cannot simply be represented by Eqs. (1.21) and (1.22) as the coherent superposition of monochromatic plane waves and the intensity integral over the wavelength and angular distributions, but the coherent superposition of partial waves over the reflected wavelength width, characteristic of the mosaic crystal, must be performed [30]. Further, the *two Gaussian distributions* of the incident neutrons observed in the interferometry experiment could be reduced to being caused by the two Gaussian distributions in the lattice spacing recently clarified for pyrolytic graphite [31].

As explained in the previous section on the double-slit experiment of Zeilinger *et al.* [24], the wave distributions were formed by the interference of partial waves with the phase difference due to the products of the wave number and optical path lengths from every incident point in the entrance slit. Then, it would be an interesting question to ask whether the coherence of waves holds or does not hold between the optical path lengths with a much larger difference, or in other words to ask how big is the path length difference or the time difference when the coherence finally disappears. Such a physical quantity expressing the maintenance of coherence in terms of spatial length is called the *coherence length*.

When we consider any experimental scheme to investigate the coherence length of a neutron, we must the first decide on whether on the incident neutrons for our device are sufficiently well approximated by monochromatic plane waves or whether they are have a wavelength distribution with a finite width. According to the principle of the Fourier integral, coherent superposition of plane waves over a finite wavelength width gives the resultant waves with a finite spatial broadening. A quite similar relation will also hold in time. Such waves localized in space or in time are called a *wave packet*. Therefore, the problem of how great is the coherence length is considered to be tightly related to the situation of how sharply the wavelength distribution is concentrated around the central value, or in other words how widely the wave packet is distributed in space and time.

However, a classical problem will arise that the propagation of waves composed of such a wavelength distribution, that is, the velocity distribution, with a finite width should be accompanied by an obvious dispersion of waves propagating to distant places. To get rid of such a dispersion, other concepts are possible in wave mechanics. One of the possible starting points is the thought that the wavelength distribution of a wave packet is the probabilistic concept of a neutron being sustained during propagation in space and time, and we observe the result of such probabilistic distributions. Experimental studies on such kinds of probabilistic concepts will be reported in the first section in Chapter 9. Another possible concept is a kind of singular wave packet inherently involving some physical structure persisting against the dispersion with the wavelength distribution. Such a singular wave packet will be studied in the last section in Chapter 9.

Therefore, here we do not go into detail on the problem of coherence and the concepts on the wave packet for a neutron, and we will study them in detail in Chapter 9.

1.3.2 Pendellösung Interference

Now, we introduce one of the early experiments estimating the *coherence length* of neutrons. Shull [32] carried out a very high precision experiment at Brookhaven National Laboratory with a neutron wavelength width of 0.0072 Å as shown in Figure 1.6a. This consisted of a thin silicon single crystal cut perpendicularly to the (111) reflection planes and fine entrance and exit slits with a width of 0.13 mm on each side of the crystal. The entrance side was illuminated with neutrons at incident angle θ very near the Bragg angle θ_B. This is the well-known setup of X-rays referred to as the *Pendellösung interference* experiment.

In this kind of *symmetry Laue diffraction* (refer to Section 6.1), the momentum component parallel to the reflecting lattice planes of incident neutrons is conserved during the propagation, whereas the perpendicular component experiences a number of Bragg reflections. As a result of the regular lattice effect and the potential effect of the crystal as a whole, with the refractive index given by Eqs. (1.14)–(1.17), and in the case of the incident angle θ with a very slight deviation from the Bragg angle θ_B, that is, at a very small deviation $\delta\theta = \theta - \theta_B$, the waves in the crystal become two split components with slightly different propagating velocities and are transported in two symmetrical directions with a small angle $\pm\epsilon$ to the Bragg angle. The transportation angle ϵ and the intensity I can be described by the equations ([32]; textbook [D] p. 431; textbook [I] Chapter 6, Section 6.3; [33] Chapter 6, Section 6.3; [34] pp. 201–202)

$$\gamma = \frac{\tan\epsilon}{\tan\theta_B} = \frac{\Delta\delta\theta/2d}{\sqrt{1+(\Delta\delta\theta/2d)^2}}\,, \tag{1.25}$$

$$I(\gamma) \cong (1-\gamma^2)^{-1/2}\sin^2\left[\frac{\pi}{4} + \frac{\pi t}{\Delta}(1-\gamma^2)^{1/2}\right]\,, \tag{1.26}$$

where d is the lattice spacing in the crystal, t is the crystal thickness, $\Delta = \pi\cos\theta/NbF_{hkl}\lambda$, N is the number of unit cells per unit volume, b is the scattering amplitude of the nucleus, and F_{hkl} is the *crystal structure factor* per unit cell contributing the reflection with the Miller indices hkl.

In Eq. (1.25), we can see that at the exact Bragg incident angle, becoming $\pm\epsilon = 0$, the perpendicular components constitute standing waves, and therefore the waves are transported in parallel to the Bragg reflection planes. However, in all cases two split waves after being propagated through the crystal with slightly different velocities emerge from the exit surface of the crystal, thus a certain phase difference in proportion to the crystal thickness results between these two components. For a sufficiently narrow entrance slit, waves after the entrance slit extend over a wide angle, then the phenomena mentioned above spread widely inside the crystal and thus the Pendellösung interference due to the split-wave interference is observed. Figure 1.6b indicates such results of the Pendellösung interference for three different values of crystal thickness observed at the center of the exit surface of the crystal

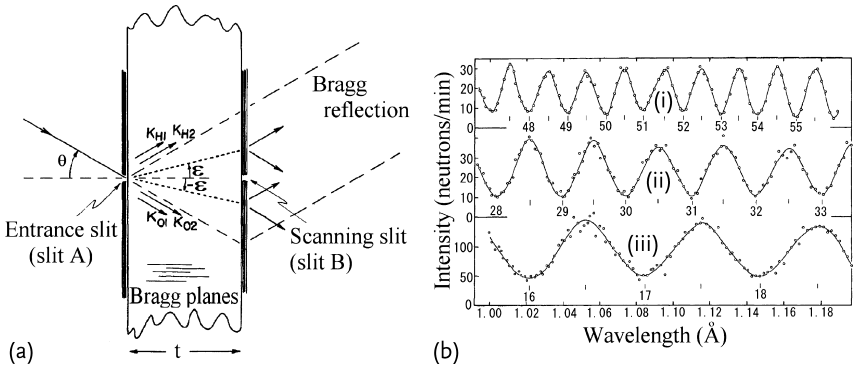

Figure 1.6 Pendellösung interference for neutrons. (a) The experimental setup; (b) fringe development at the center of the Bragg reflection as the wavelength increase for the crystal with the thickness; (i) 1.0000 cm, (ii) 0.5939 cm, (iii) 0.3315 cm (Shull [32]).

on minutely varying the incident neutron wavelength. From the order number of the *interference fringes* shown in Figure 1.6b, sufficiently high contrast is observed beyond 55th order. After the correction of the finite experimental resolution, the loss of contrast becomes of the order of 2% or even less, and thus the *coherence length* of neutrons in the present experiment was estimated to be larger than 2750λ, or 0.3 μm.

Further, interference variations induced by more effective and different kinds of phase shifts are observed for neutron waves by making use of various kinds of neutron interferometers, and the results will be described in Chapter 9.

1.4
Corpuscular Properties of the Neutron

1.4.1
Time-of-Flight Analysis

As early as a few years after the discovery of the neutron by Chadwick in 1932, it was experimentally assured that this neutral particle with mass much greater than that of the electron could be slowed down to the room temperature energy region by scattering by nuclei. For example, Dunning *et al.* [35] measured the time of flight of the neutrons emerging from the surface of a cylindrical paraffin block 16 cm in diameter and 22 cm long, in the center of which a 600 mCi Rn–Be neutron source was embedded. For the measurement they used the transmission through a couple of rotating absorber discs with slits. The two discs, each having a slit with an opening angle of 3.7° and provided with a similar fixed disc, were 54 cm apart and connected to each other with a lag angle of 3.5°. The device thus works as a *mechanical velocity selector* for neutrons in which neu-

trons with a velocity corresponding to the rotation speed are able to pass through the device. The count rates plotted against rotation speed agreed well with the Maxwellian distribution, having the maximum intensity at a neutron speed of about 2300 m/s.

The *flight velocity* of neutrons thus measured represents the particle motion of the neutrons, and at the same time it corresponds to the group velocity in the wave mechanics as mentioned in Section 1.1. The wavelength given by Eq. (1.9) for neutrons with energy corresponding to room temperature is on the order of interatomic distances, indicating possible applicability of these neutrons to spectroscopy experiments for material physics, but the neutron intensity as well as the energy resolution of the experimental arrangement of Dunning *et al*. were not sufficiently high for such applications. The precise time-of-flight spectroscopy for neutrons was carried out first by Alvarez, as shown in Figure 1.7a, by making use of a cyclotron to accelerate deuterons to be injected into a beryllium target and the neutrons pro-

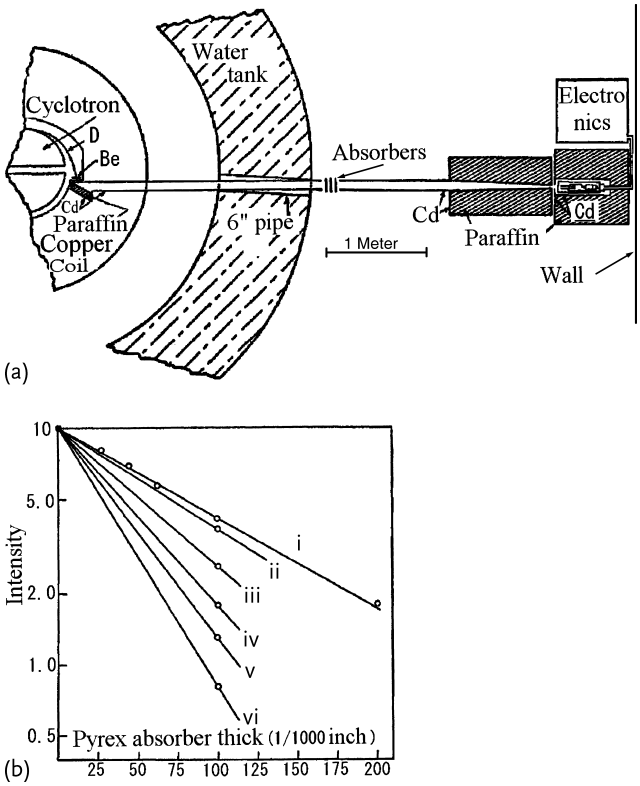

Figure 1.7 Time-of-flight spectroscopy experiment with time-modulated operation of a cyclotron; (a) Plan of cyclotron room; (b) Boron absorption variation with timing scheme, abscissa; absorber thickness, ordinate; transmitted neutron intensity (normalized), i: continuous measurement, ii–vi: delay time increased by about 1/240 s per step. (Alvarez [36]).

duced were moderated in a paraffin block. For the velocity analysis of moderated neutrons, he used the *electrical velocity selection* method with time-modulated operation for deuteron acceleration and synchronized control of the neutron measuring system [36].

There were several severe tasks and difficulties in the controlled operation of the cyclotron beyond 100 Hz to achieve thermal neutron spectroscopy, but finally the energy selection of neutrons around 300–10 K could be well achieved with the modulated operation at 120 Hz. From the measurements of the transmission ratio of such velocity-selected neutrons, the $1/v$ law, v being the neutron velocity, on the absorption cross section of boron was confirmed, as shown in Figure 1.7b.

The performance of the 1.5 m cyclotron used in the neutron experiment at Berkeley, the University of California, gave a deuteron energy of 8 MeV, a deuteron current of 50–60 μA in the steady-state operation, and 5–10 μA in the modulated operation at 60 Hz.

Later, in 1940, Baker and Bacher reported a *time-of-flight experiment* similar to the Alvarez one but with a much higher repetition frequency, that is, a period of 2500 μs, a neutron burst width of 50–100 μs, and a modulation time accuracy of 5 μs [37]. In the same year, Alvarez *et al*. carried out a magnetic resonance experiment for neutrons with the steady-state operation of the cyclotron; this will be described in the next section.

I would like to insert a short description of the activities in Japan during similar periods. Kikuchi *et al*. constructed a cyclotron with an accelerated deuteron energy of 4.2 MeV in the central Osaka campus opened in 1932, of Osaka University, and started nuclear physics studies with it. However, the outbreak of the Second World War unfortunately disturbed and finally interrupted the continuation of the research in the 1940s. Independently, at the Science and Chemistry Institute in eastern Japan, Nishina constructed a 1.5 m cyclotron in 1943 for nuclear physics studies. At Kyoto University, the construction of a cyclotron was started. All these experimental activities in nuclear and neutron physics in Japan were stopped at the end of the Second World War owing to the destructions of the facilities by the occupation forces. Thereafter, experimental neutron research in Japan recovered, accompanied by the development of research reactors and high-intensity accelerators after the 1960s.

Experimental research on neutrons after the 1950s progressed remarkably by making use of research reactors developed in the United States and in Europe. Further, after the 1970s, with the construction of high-flux reactors, various kinds of advanced neutron spectroscopies were proposed and practically applied to neutron optics and condensed matter studies. Furthermore, the successful developments of high-intensity accelerator sources in Europe and the United States promoted pulsed neutron experiments as a competitive approach to continuous beam experiments. Nowadays, the most intense pulsed neutron sources are constructed in the United States and in Japan and are starting their operations. Some of the wide variety of neutron optics and spectroscopy developments as well as their applications will be introduced in the following parts of this book.

1.4.2 From a Particle to a Wave

One of the very interesting investigations in Munich relating to the particle motion of neutrons reflected by a mirror will be described here. If the reader has some difficulty in understanding well the explanations, the information given in the next chapter will help gain a better understanding.

To understand deeply the wave–particle duality in the phenomenon of neutron reflection on a mirror, Felber *et al*. undertook a comparison between the results of the *classical mechanical analysis on the reflection of a particle beam* and of the *quantum mechanical analysis on the reflection of matter waves*, and studied the possible transition from the former to the latter under the developments of temporal and energy conditions in the reflection [38]. Practically, they considered the reflection of *very cold neutrons* with a wavelength of 2.4 nm on a surface vibrating at high frequency, and compared the theoretical analyses with the experimental results carried out at the Munich and at the Geesthacht research reactors. They succeeded in indicating the transition of the time-dependent reflection phenomenon from classical to quantum mechanical according to the developments of frequency and amplitude parameters with the surface vibration.

The vibrating mirror surface is represented by a *step potential* with height V_p under one-dimensional motion with amplitude a_p and angular velocity ω_p. The collimated neutrons with energy E_0 (the wave number k_0, velocity v_0) experiencing such a potential can be classified according to the values for three parameters $\alpha = 2k_0 a_p$, $\beta = V_p/E_0$, and $\gamma = a_p \omega_p / v_0$.

In the framework of the classical description, the neutron trajectory should be calculated iteratively by solving the equation of motion successively after every collision, but the neutron velocity change due to the collision necessary to obtain the neutron flux is given in an implicit form; therefore, the solution can only be found numerically.

In the framework of the quantum description, on the other hand, it is enough to introduce the step potential in the time-dependent Schrödinger equation, but our case is essentially different from the usual cases given in many textbooks, since our *potential is time-dependent*. Felber *et al*. therefore started with the expansion of the wave function into the *partial waves* with the number of transferred phonons n, and then investigated the behavior of the analytical solutions for the particle waves in the extreme cases for the parameters (small amplitude; $\alpha \ll 1$, or quasi-stationary; $\gamma \ll 1$) and further were able to calculate the approximate solutions for other general cases up to the order of the expansion $|n_{\max}| = N \cong 2\alpha$ to satisfy the required accuracy.

The results of these calculations are shown in Figures 1.8 and 1.9. From Figure 1.8a and b, we understand the quantum effects become significant for $\alpha < 10$, whereas for $\alpha \gg 10$ the results approach those of classical mechanics. Further, in Figure 1.8c, we recognize many black bars for the quantum reflections in the region where no reflections are expected in classical mechanics, that is, no black continuous spectrum is shown. Therefore, all of these reflections in $E' < 0.5$ in

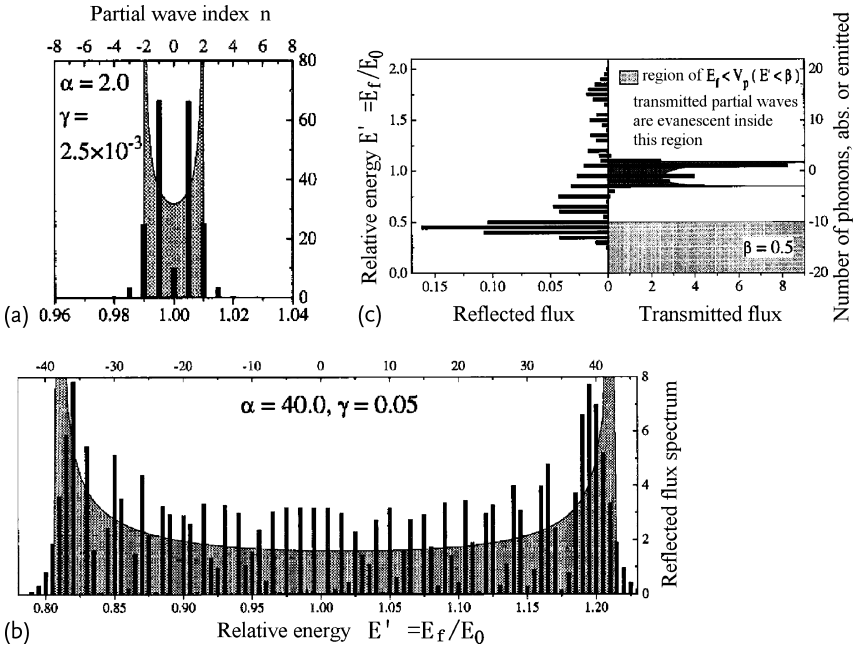

Figure 1.8 Comparison between the calculated results on a particle beam and on matter waves: (a) and (b) the case of the parameter value for $\beta = 10$, and the value for α varied (classical; gray patterns, quantum; black bars); (c) reflected and transmitted distributions for $\alpha = 15.0$, $\beta = 0.5$, $\gamma = 0.1875$ (classical; black pattern, actually no results for this parameter value, quantum; black bars, the gray region indicates the potential height) (Felber *et al.* [38]).

Figure 1.8c indicate quantum particle reflections. The comparison with their experiments are shown in Figure 1.9, where Figure 1.9a shows the experimental setup of the *reflection experiment with the vibrating mirror*.

Since the neutron velocity component parallel to the mirror surface $v_{0\|}$ is conserved, the situation can be reduced to a one-dimensional problem in which the previous parameter values are replaced by the corresponding relations for the perpendicular component $v_{r\perp}$. Thus, the energy and the velocity changes of neutrons reflected by the vibrating mirror described in Figure 1.8 are equal to the changes of the perpendicular components $E_{r\perp}$ and $v_{r\perp}$, respectively, and the resulting change of the reflection angle θ_r will be observed according to the relation

$$\tan\theta_r = \frac{v_{r\perp}}{v_{0\|}} = \tan\theta_0 \sqrt{1 + \frac{\Delta E_\perp}{E_{0\perp}}}\,, \tag{1.27}$$

where $E_{0\perp} = E_0 \sin^2\theta_0$ and $\Delta E_\perp = E_{r\perp} - E_{0\perp}$. Figure 1.9b shows the experimental results for various values of the parameter α and compared with those of the matter wave calculations, where $1\,\text{neV} = 10^{-9}\,\text{eV}$. We can conclude that both results agree well by considering the effects of the finite resolution included in the experimental results

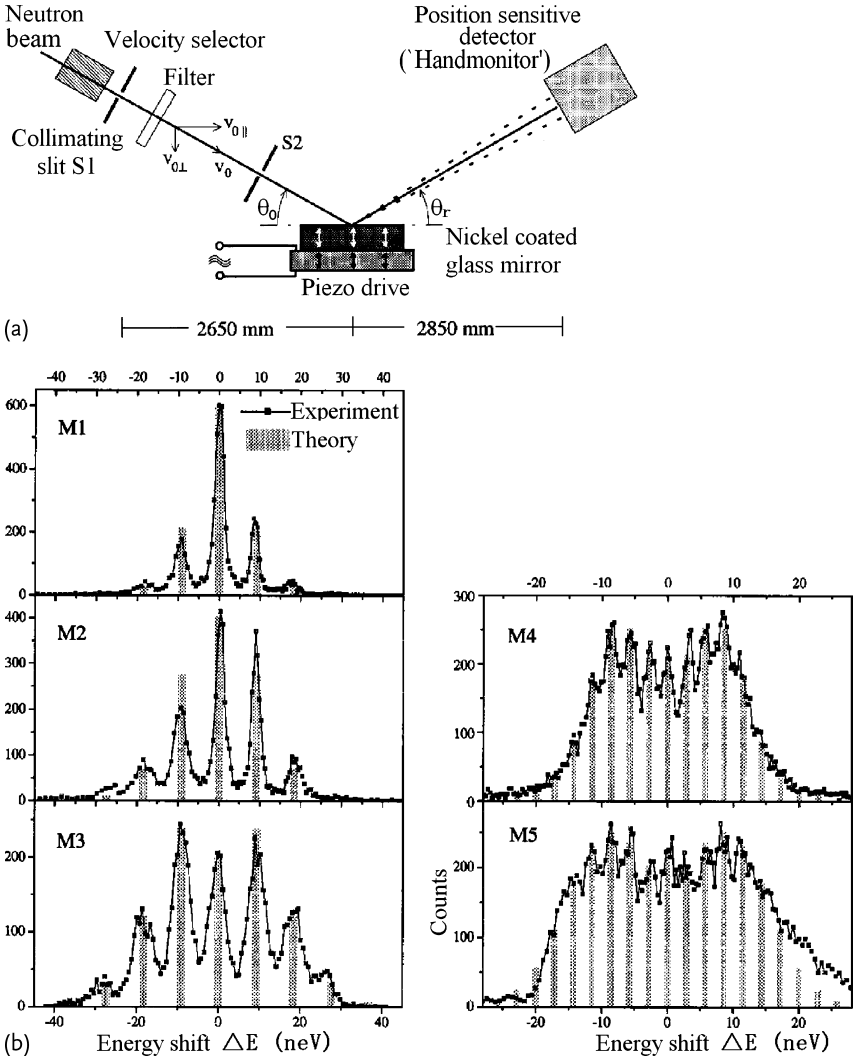

Figure 1.9 (a) Arrangement (incident wavelength $\lambda = 2.4$ nm, incident angle $\theta_0 = 2.00°$); (b) experimental results compared with calculations, Experimental results: Abscissa, energy transfer estimated from the change of reflection angle; Ordinate, reflected neutron counts; From M1 to M5, modulation index α increases, that is, M1–M3; $\alpha = 0.95, 1.45, 1.98$ (frequency $f = 2.2206$ MHz); M4, M5; $\alpha = 4.21, 5.82$ (frequency $f = 0.69295$ MHz), (Felber *et al.* [38]). (b) Reflection experiment of very cold neutrons on a vibrating mirror.

From the transition shown in Figure 1.8 from a few discrete spectra to the continuous spectrum for increasing the value for α, that is, in the transition from quantum mechanics to classical mechanics as shown in Figure 1.8, the analytical method appropriate for a given condition can be decided from the parameter values.

1.5 Magnetic Moment of the Neutron

The neutron has *spin* 1/2 and the *magnetic dipole moment* $\mu_n = -1.91\mu_{\mathrm{NB}}$, where μ_{NB} is the *nuclear magneton* $e\hbar/2Mc$, defined for the proton mass M. The half-integer neutron spin was predicted from the structure of a deuteron on the discovery of the neutron by Chadwick. Soon after, in 1937, it was confirmed, together with the spin dependence of the neutron–proton internucleon interaction, by the measurement and the analysis on the diffusion characteristics of thermal neutrons in liquid hydrogen samples with different ratios of two kinds of hydrogen molecules, orthohydrogen and parahydrogen [39, 40]. On the other hand, the magnitude of the neutron magnetic moment was determined from the measurement of neutron spin behavior in a magnetic field, which will be described next.

1.5.1 Spin Flip in Magnetic Resonance

A spin with magnetic moment μ precesses in a magnetic field with the *Larmor precession frequency* $\nu_L = 2\mu H/h$ around the direction of the magnetic field, the motion being called the *Larmor precession*. For a particle with a half-integer spin in a magnetic field, the theoretical formula for the spin reversal probability at time t in the situation of *nonadiabatic spin flip* was derived by Güttinger [41], who solved the Schrödinger equation for a spin-1/2 particle in a magnetic field rotating with frequency ν. His formula is given for the case where the rotational axis of the magnetic field makes an angle $\vartheta = \pi/2$ with the direction of the field. A more general formula was given by Rabi [42] for an extended condition of the *total magnetic field* H, to be decomposed into a *static magnetic field* H_0 and a *rotating magnetic field* with magnitude H_1 perpendicular to the direction of H_0. His formula, Eq. (1.28), applicable to an arbitrary value for the polar angle ϑ between the directions of H and H_0, is written as

$$P_{\left(\frac{1}{2},-\frac{1}{2}\right)} = \frac{\sin^2\vartheta}{1+q^2-2q\cos\vartheta}\sin^2\left[\pi\nu t\sqrt{1+q^2-2q\cos\vartheta}\right], \tag{1.28}$$

where $P_{\left(\frac{1}{2},-\frac{1}{2}\right)}$ denotes the probability that the spin state initially at $+1/2$, that is, polarized in the direction of the total field at time $t = 0$, becomes the $-1/2$ state at time t, and $q = \nu_L/\nu$. Putting $\vartheta = \pi/2$ in Eq. (1.28) gives the same result as with Güttinger's formula.

Since the terms as a function of q on the right side of Eq. (1.28) can be rewritten as $1 + q^2 - 2q\cos\vartheta = (q - \cos\vartheta)^2 + \sin^2\vartheta$, the *resonance condition for spin flip* in which $P_{\left(\frac{1}{2},-\frac{1}{2}\right)}$ takes the maximum value is given by $q_{\mathrm{res}} = \cos\vartheta$. Then, the spin flipping probability at that condition follows the time dependence

$$P_{\left(\frac{1}{2},-\frac{1}{2}\right)\mathrm{res}} = \sin^2(\pi\nu t\sin\vartheta)\,; \tag{1.29}$$

therefore, the probability will approach unity if we optimize the residence time of the particles inside the magnetic field. Furthermore, there being two kinds of rota-

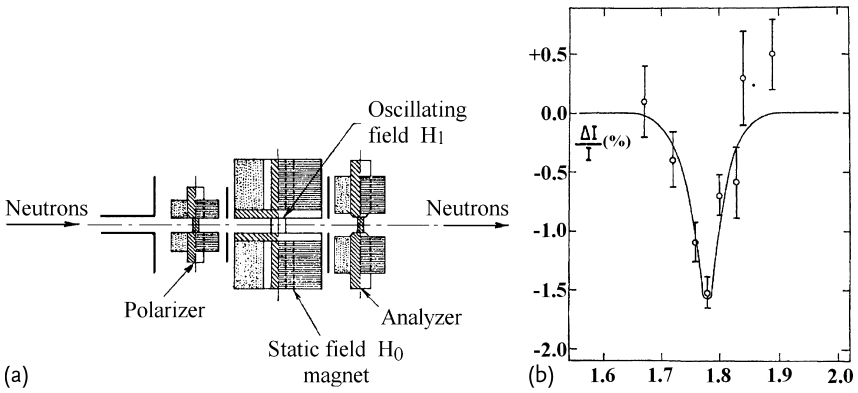

Figure 1.10 Magnetic resonance experiment for the neutron: (a) experimental apparatus; (b) count rate decrease observed at the resonance. The abscissa represents the magnetic field current in arbitrary units (Alvarez and Bloch [43]).

tion direction, that is, clockwise and counterclockwise, with the same magnitudes of frequencies ν_L and ν, the resonance condition in Eq. (1.28) requires not only the magnitude but also the sign of ν to match those of ν_L.

In other words, we can determine whether the magnetic dipole moment of the particle is positive or negative from the magnetic resonance experiment by making use of a *rotating magnetic field*, but this is not possible if we use the *reciprocating magnetic field*, which is the superposition of clockwise and counterclockwise rotating fields.

An experiment using this *nuclear magnetic resonance method* applied to neutrons was carried out by Alvarez and Bloch with the insertion of the resonance apparatus shown in Figure 1.10a in the cyclotron described earlier, and the *magnetic dipole moment of the neutron* was derived from their experiment [43]. In their experiment, the cyclotron was operated in a steady-state mode, which was advantageous from the viewpoint of the background effects in comparison with those in the modulated operation mode.

For the *polarization* of the incident neutrons and also for the *polarization analysis* of neutrons transmitted through the resonance apparatus, the *transmission method with magnetic scattering* through several centimeter thick iron plates magnetized by wires carrying electric currents was used. Further, they employed the method to find the resonance condition from the maximum of $P_{(\frac{1}{2},-\frac{1}{2})}$ by varying the static magnetic field H_0 under a constant frequency $\nu_n = \omega_n/2\pi$ of the oscillating magnetic field, assuming that the second term on the right side of Eq. (1.28) should be averaged over owing to the broad distribution of the residence time in the magnetic field of neutrons with various velocities. Furthermore, they used the resonance spin flip formula for the initial condition polarized in the direction of the static field, based on the small H_1/H_0 ratio, actually smaller than 2% for a static magnetic field H_0 of 600 G and an oscillating field strength H_1 of about 10 G.

The homogeneity of the magnetic field H_0 in the experiment of Alvarez and Bloch was 600 ± 1 G over the whole of the resonance region, and the voltage fluctuations of the magnet power supply were maintained below 0.1% by the control system compensating the effect due to the coil temperature variation. To determine precisely the number $\bar{\mu}_n$ which corresponds to the neutron magnetic moment μ_n expressed in the unit of *nuclear magneton*, $e\hbar/2Mc$ (M is the proton mass), they employed the method to compare the *resonance angular frequency* ω_n for the neutron in a *magnetic field* of strength H_n with the *resonance angular frequency* for the proton ω_p accelerated by the cyclotron, according to the equations

$$\omega_n = 2H_n\mu_n/\hbar = (2H_n\bar{\mu}_n/\hbar)(e\hbar/2Mc) = (eH_n/Mc)\bar{\mu}_n\,, \tag{1.30}$$

$$\omega_p = eH_p/Mc\,, \tag{1.31}$$

$$\bar{\mu}_n = (\omega_n/\omega_p)(H_p/H_n)\,. \tag{1.32}$$

One of their experimental results for the resonance curve is shown in Figure 1.10b for the magnetic field frequency $\nu_n = 1.843$ MHz.

As the final result of these measurements repeated many times, the *neutron magnetic dipole moment* in the unit of nuclear magneton was determined as

$$\bar{\mu}_n = -1.93_5 \pm 0.02\,. \tag{1.33}$$

Although the sign of the magnetic moment for the neutron could not be determined in the experiment, where a reciprocating field was used, it had already been deduced to be negative from the *Stern–Gerlach magnetic deflection experiment* for protons and deuterons by Stern *et al*. [44, 45].

The main experimental efforts to determine precisely such a physical constant in these early neutron experiments by making use of accelerators were devoted to the stability and reproducibility of the measurements, especially with Alvarez *et al*. having had difficulty to achieve the required stable operation of the cyclotron (a fluctuation of the magnet source voltage below 0.1%). By the way, the experiment to determine directly the sign of the neutron magnetic moment by making use of two *mutually orthogonal magnetic fields* was later carried out by Rogers and Staub [46].

The phase difference between the incident and the exit neutron spins during the resonance will be accumulated over the period of Larmor precession and thus the accuracy of the phase determination will be improved in proportion to the number of precessions. *Ramsey's separated oscillating magnetic field method* [47] in which the oscillating field is split into two widely separated locations along the neutron flight path and a constant precession field is provided in the flight path between the separated fields for the continuation of the Larmor precession gave an epoch-making improvement in such resonance experiments for particles as mentioned above. Corngold *et al*. performed the first resonance experiment with this method applied to the neutron in the graphite reactor at Brookhaven National Laboratory [48, 49]. The results of this experiment are shown in Figure 1.11, and combined with the result of a similar measurement on a proton sample (H_2O) with the same

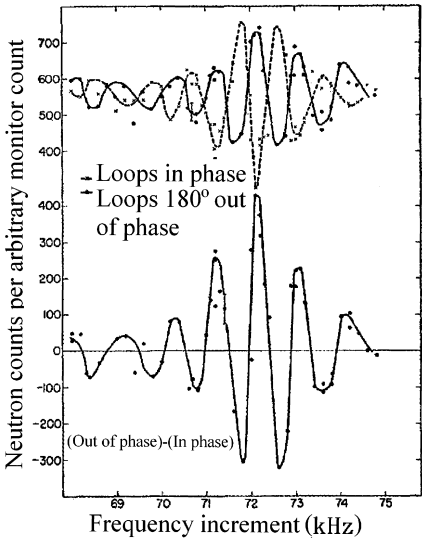

Figure 1.11 Neutron magnetic resonance experiment with separated oscillation fields method carried out by Corngold *et al.*: the upper two plots are the count rates as a function of the frequency (the resonance frequency being about 24.727 MHz) for the conditions in phase and 180° out of phase, respectively, and the lower one shows their difference (Corngold *et al.* [49]).

apparatus; this gave a much improved accuracy for the *neutron magnetic moment* as

$$\bar{\mu}_n = -1.913148 \pm 0.000066\ . \tag{1.34}$$

We add here one of the later results with further improved accuracy [50] also carried out with the separated field method:

$$\bar{\mu}_n = -1.91304308 \pm 0.00000058\ . \tag{1.35}$$

1.5.2
Adiabatic Spin Reversal in a Magnetic Gradient

The resonance phenomenon described above by making use of uniform fields has a very sharp resonance frequency, being very advantageous for precise measurements of a physical quantity of a particle. Therefore, besides the determination of magnetic moments, it is also applied to search for the *electric dipole moment* of the neutron as the most sensitive experimental method at present for verifying the possibility of the neutron having a finite electric dipole moment. However, from the viewpoint of efficient reversal of spins, Eq. (1.29) indicates the difficulty of attaining the resonance condition for neutrons with widely distributed velocities, spending different residence times in the precession field.

Another approach for spin reversal, named *adiabatic spin flip method with magnetic gradient*, is used for such cases to attain efficient performance for a wide velocity spectrum. This method of adiabatic spin reversal in a magnetic gradient consists of a static magnetic field with a gradient and an oscillating magnetic field in the middle of the static field, the working principle of which can be understood in the *rotating frame*.

Before considering the magnetic gradient method, it will be instructive to describe the experiment of Alvarez *et al*. in the *rotating frame* with the same frequency ν_n as the oscillating field around the axis in the direction of the static field. At the resonance condition where the frame rotation frequency is exactly the same as the Larmor precession frequency, the phenomenon of spin precession will disappear, that is, the effect of the static field H_n is canceled. On the other hand, the oscillating field seems to be at rest with a field strength of H_1. As a result of these transformations, the neutron spin will precess very slowly at the Larmor frequency in the field H_1 around the direction of the field H_1 now at rest in this rotating frame. The *spin flipping time*, defined as the time required for the complete spin reversal, that is, π spin turns, is just half of the Larmor precession period in this situation.

Now, we consider the magnetic field with a gradient as shown in Figure 1.12a, where the static field strength H_0 varies along the oscillating field region ($x = x_0 \sim x_1$) on the x-axis in the direction of the neutron flight. The equality $H_0(x) = H_n$ required in the previous case is satisfied only midway, $x = x_c$, in the path, and upstream the static field strength $H_0(x)$ becomes gradually larger than H_n, that is, $x_0 \leq x < x_c$; $\Delta H(x) = H_0(x) - H_n \geq 0$, where $\Delta H(x_0) \gg H_1$. Downstream, however, H_0 gradually becomes smaller than H_n, that is, $x_c < x \leq x_1$; $\Delta H(x) \leq 0$, where $|\Delta H(x_1)| \gg H_1$. At the entrance ($x = x_p$) and the exit ($x = x_a$) positions of the device, there is a neutron polarizer and a polarization analyzer.

With a similar transformation to the rotating frame as previously considered, during the passage in the upstream region starting from the entrance to the mid-

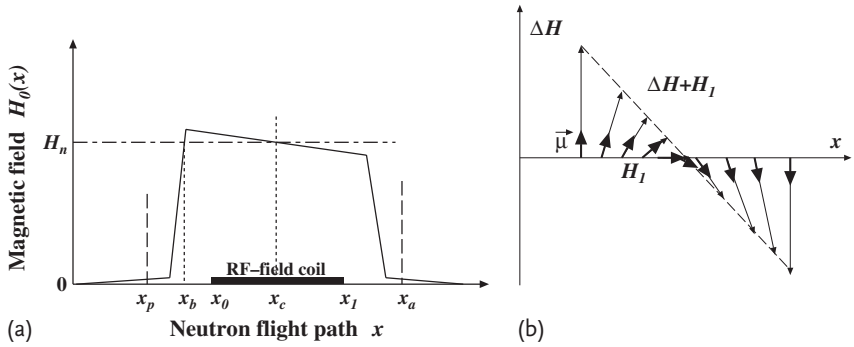

Figure 1.12 Description of the adiabatic spin flip method with a magnetic gradient: (a) setup and field distribution; (b) movement of the field direction followed by a spin vector adiabatically in a rotating frame synchronous with an oscillating magnetic field.

way position, where $\Delta H(x) > 0$, the neutron spin follows the motion of the magnetic field described as $\boldsymbol{H}_{\text{eff}}(x,t) = \Delta H(x)\boldsymbol{e}_z + H_1\boldsymbol{e}_{x'}$, where $\boldsymbol{e}_{x'}$ denotes the direction of H_1 at time t; thus, as shown in Figure 1.12b it results that the spin parallel (or the spin antiparallel) to H_0 at the entrance moves to the direction parallel (or antiparallel) to H_1 at the midway position, and further in the downstream region continues to move to antiparallel (or parallel) to H_0 as the sign of $\Delta H(x)$ reverses. In this way, regardless of the initial spin direction, the spin reversal is attained quite smoothly for a wide range of the neutron velocity. This is the principle of adiabatic spin flip with a magnetic gradient.

The velocity region of the neutrons for which the spin flipping mechanism mentioned above works well will be defined as follows.

First, the *adiabatic spin flip condition* requires the *adiabatic following after the magnetic field*, that is, the direction of the magnetic field in the device (now we consider it in the rotating frame), moves sufficiently slowly compared with the angular velocity of the Larmor precession in the magnetic field H_1. This can can be expressed as

$$\begin{aligned} &\frac{v_{n\max}}{H_1}\left|\frac{dH(x)}{dx}\right| \ll \frac{2|\mu_n|H_1}{\hbar}\,, \\ \text{or}\quad &v_{n\max}\left|\frac{dH(x)}{dx}\right| \ll \frac{2|\mu_n|H_1^2}{\hbar}\,, \quad x_0 \le x \le x_1\,, \end{aligned} \tag{1.36}$$

where μ_n is the magnetic dipole moment of a neutron, and $v_{n\max}$ denotes the maximum velocity for the neutrons performing the adiabatic spin flip.

Next, in addition to the midway position, there is another point, either at the entrance or at the exit (in the case in Figure 1.12a it is the entrance side), where the equality $H_0(x) = H_n$ holds at the position $x = x_b$. For successful working of the spin flip mechanism for the neutrons transmitted through the device, any additional spin reversal should not occur at this point of $x = x_b$, otherwise the spin would return back to the initial state. Since the oscillating field produced by the coil extending over the region $x = x_0 \sim x_1$ in the device should leak out somewhat to the point x_b, we have to make the field gradient around $x \cong x_b$ so steep that the turning speed of the local field direction becomes much faster than the Larmor precession of the spin at that location. This additional condition is written as

$$\begin{aligned} &\frac{v_{n\min}}{H_1}\left|\frac{dH(x)}{dx}\right|_{x=x_b} \gg \frac{2|\mu_n|H_1}{\hbar}\,, \\ \text{or}\quad &v_{n\min}\left|\frac{dH(x)}{dx}\right|_{x=x_b} \gg \frac{2|\mu_n|H_1^2}{\hbar}\,, \quad x \cong x_b\,, \end{aligned} \tag{1.37}$$

where $v_{n\min}$ denotes the minimum velocity for the neutron getting rid of such an additional spin reversal.

As a result of these requirements, the adiabatic spin flip will be attained successfully for neutrons in the rather wide velocity region defined by Eqs. (1.36) and (1.37).

The experimental study on the spin flipping characteristics with the gradient field adiabatic method was carried out by Egorov *et al.* [51], who measured the

transmitted intensity and its static field dependence of very slow neutrons (*ultracold neutrons*) with a velocity below about 20 m/s through the spin flip device with a configuration similar to that shown schematically in Figure 1.12a. The ultracold neutrons were extracted from the curved guide tube at the VVR-M reactor of the St. Petersburg Nuclear Physics Institute. For the polarization and the polarization analysis, the transmission method of magnetized materials was employed (the setup was similar to that shown in Figure 1.10a), but in the present case for ultracold neutrons they used the *polarizer* and *analyzer* with a *magnetic reflection method* on a thin film, that is, a 1 μm thick evaporated iron layer, instead of the magnetic scattering method for thermal neutrons used by Alvarez. An oscillating field with a frequency 200 kHz, and a resonance field current of about 510 mA gave the resonant decrease of the neutron count rate down to about half with a resonance half width of about 3 mA [51].

Further, Ezhov *et al.* performed a comparison of the gradient field adiabatic method and Ramsey's resonance method in the case of bottled ultracold neutrons (refer to Section 2.2.2) experiencing Larmor precession in the bottle over a period of about 4.6 s on average. As mentioned already, the latter method is often used for the precise measurement of the resonance condition, such as for studying the existence of the electric dipole moment of the neutron. They carried out Monte Carlo calculations on the spin flipping performances in both methods mentioned above. The spin flip spectrometer had two separated oscillating fields at the entrance and the exit sides of the precession space in a homogeneous static field. Their comparisons of the calculated results for both methods are shown in Figure 1.13a, in which an about 1.8 times higher polarization ratio for the gradient field adiabatic

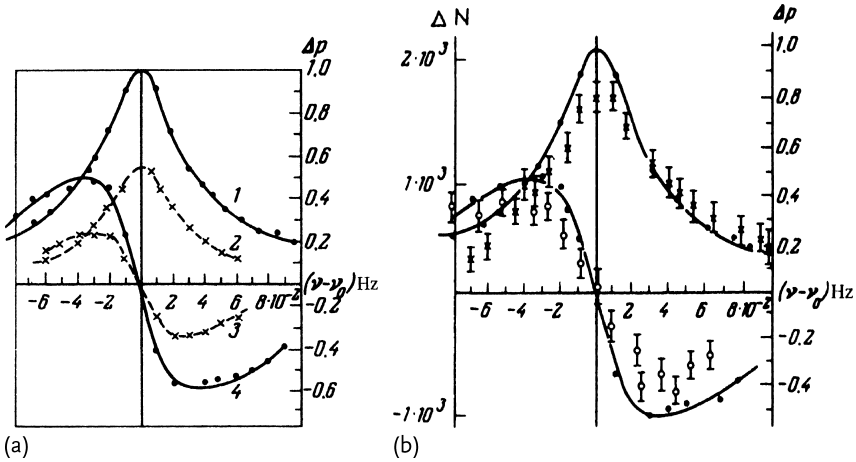

Figure 1.13 Comparison between the spin flipping characteristics for ultracold neutrons with the gradient field method and with Ramsey's resonance method. (a) Results of numerical calculations; the solid curves represent the gradient field method, whereas the broken curves represent Ramsey's method. Curves 1 and 2 are for phase differences of 0° and 180° and curves 3 and 4 are those for phase differences of 90° and 270°. (b) Comparison with experimental results for the gradient field method (Ezhov *et al.* [52]).

method is indicated in comparison with Ramsey's resonance method. The feasibility of the correctness of the calculated values for the gradient field adiabatic method is also illustrated in Figure 1.13b as a comparison with the measured values, which show satisfactory agreement with the calculated values.

Herdin *et al*. also carried out the polarization experiment with the adiabatic spin flip method for ultracold neutrons with a velocity below about 8 m/s passing through a guide tube, in which a high spin-flipping efficiency of about 100% with a statistical error of 2% and a polarization efficiency of 95–98% for the neutron velocity region of 4.15–8.2 m/s were achieved [53].

The neutron spin precession in a magnetic field studied as described above can be applied for the development of neutron spectroscopies, and various kinds of high-resolution neutron spectrometers have been developed by utilizing these characteristics of Larmor precession. The first idea in this direction was suggested and developed by Mezei in 1972 [55], this new principle being named *neutron spin echo spectrometry* (see the schematic arrangement shown in Figure 1.14). It opened the door to the wide field of neutron spin spectroscopy. Generally speaking, neutron spectroscopy experiments are carried out to study the energy structures and their characteristics in a sample from the experimental results for the *transferred energy* as the difference between the incident and scattered neutron energies. Thus, for high-resolution investigations on the energy structures, similarly high-resolution analyses of the transferred energy are required.

The conventional spectroscopy method is based on wavelength or velocity spectrometry; time-of-flight spectrometry suffers from the serious intensity loss accompanying the severe selection of the incident neutrons needed to satisfy the requirement of such a high-energy resolution. In contrast, in the new principle of neutron spin echo spectroscopy, the information on the neutron energy does not require

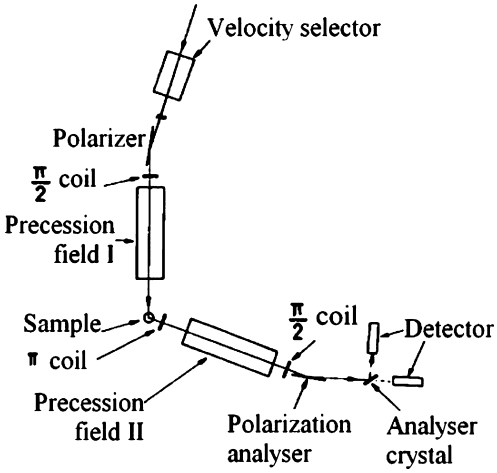

Figure 1.14 Schematic layout of neutron spin echo spectrometer. Typical lengths of the precession field regions are 2–4 m (Mezei [54]).

wavelength or velocity spectrometry, but is labeled on the neutrons as the number of Larmor precessions. A practical and basic configuration of the neutron spin echo spectrometer is shown in Figure 1.14. During their flights through the incident and scattered flight paths with, respectively, well-defined path lengths and well-defined magnetic field strengths, neutrons experience Larmor precessions; thus, after the flights the number of precessions is labeled on individual neutrons. It is quite possible to reverse the sign of the precession number, that is, label a negative number for the precession after the scattering by a sample, by reversing the direction of the magnetic field or by reversing the neutron spin. Then the resultant number of precessions observed at the end of the flight will be given by the difference between those of the incident and the scattered paths, $\Delta N \cong N\delta\nu/\nu$, where $\delta\nu = \nu' - \nu$ denotes the difference between the incident and the scattered neutron velocities. In this way, we need not select the incident neutron velocity within a very narrow width in proportion to the very high resolution of the velocity change $\delta\nu$, but we can obtain as high a velocity resolution $\delta\nu$ as we wish by increasing the number of precessions N to satisfy the present relation under a given resolution ΔN in the experimental device. The present principle of echo spectrometry and the utilization of a much wider energy width than in conventional spectrometries are the important advantages of high-resolution spectroscopy with the neutron spin echo method.

We would like to add here a little advanced detail on another important characteristic of the neutron spin echo method. In conventional spectroscopy, the scattered intensity distribution $I(Q,\epsilon)$ is usually obtained for the transferred energy ϵ in inelastic and quasi-elastic neutron scattering experiments, whereas in the spin echo method the measured neutron intensity is given by the scattering function $S(Q,\epsilon)$ integrated over ϵ with the weight of the polarization analysis component $P_x = \cos(2\pi N\delta\nu/\nu)$ on the energy transfer structure in the sample. As supposed from the principle of the Fourier integral, the latter means that we can directly obtain data concerning the time-correlation function on the dynamical structure in the sample. Further details on the developments of spin echo spectrometers will be given in Chapter 3.